Research Article Vol. 4, No. 2 / 15 Feb 2025 / Optics Continuum 382
OPTICS CONTINUUM

Correcting spurious apodization effects in digital holographic microscopy using a simple Fourier transform spectrometer

JONGSU KIM,[1] TAMAR VAN GARDINGEN-CROMWIJK,[2,3,*] MARC NOORDAM,[2,3] MANASHEE ADHIKARY,[4] JOHANNES F. DE BOER,[2,3] CHANGMIN PARK,[1] YOUNGSEOK KANG,[1] AND ARIE DEN BOEF[2,3,4]

[1]*Samsung Electronics Co., Ltd., 1, Samsungjeonja-ro, Hwaseong-si, Gyeonggi-do, 18448, Republic of Korea*
[2]*Advanced Research Center for Nanolithography (ARCNL), Science Park 106, 1098 XG Amsterdam, The Netherlands*
[3]*Department of Physics and Astronomy, and LaserLaB, Vrije Universiteit, De Boelelaan 1081, 1081 HV Amsterdam, The Netherlands*
[4]*ASML Netherlands B.V., De Run 6501, 5504 DR, Veldhoven, The Netherlands*
[*]*t.cromwijk@arcnl.nl*

Abstract: The use of quasi-monochromatic light in digital holographic microscopy can lead to spurious apodization effects. The resulting image degradation can be corrected by compensating for this effect if the spectrum of the light source is known. Here, we present a simple Fourier-transform spectrometer that accurately measures the spectrum of a quasi-monochromatic light source. We will present measured spectra, obtained with this FT spectrometer, and we will show how these spectra can be used to computationally correct for spurious apodization effects. The resulting improvement of image quality is especially of interest for optical metrology applications that require high-quality imaging performance like overlay metrology.

1. Introduction

Digital holographic microscopy (DHM) is an established and well-known microscopy technique whose value has been demonstrated in many application domains ranging from biology [1] materials science [2,3] and metrology [4]. Several papers have reported the potential benefits of dark-field DHM for overlay metrology in the semiconductor device manufacturing [5–8]. For this application, DHM is used to make high-resolution images of dedicated small overlay targets on a wafer. Due to the continuous shrink of device features, the precision requirements for overlay metrology are well in the sub-nanometer range, driving the need for near-perfect imaging over a large range of wavelengths. For example, Ref. [9] shows the capability to correct for non-isoplanatic aberrations and Ref. [5] demonstrates the capability of DHM to measure overlay from visible to short-wavelength IR (SWIR) wavelengths. Finally, in Ref. [7] we presented the benefits of DHM for measuring overlay on very small overlay targets. Despite the advantages of this coherent imaging system, it has been shown in Ref. [10] that the use of quasi-monochromatic light in dark-field DHM can lead to an undesired spurious apodization of the spatial frequency spectrum of the image. Since metrology targets typically have dimensions of about $10 \times 10\ \mu m^2$ and are often surrounded by other structures, a near-perfect aberration-free imaging performance with a localized point-spread function (PSF) is required. The spurious apodization, i.e. pupil amplitude variation, affects the PSF. The resulting degradation of the imaging quality can potentially lead to errors in the retrieved overlay. In Ref. [10] the spurious apodization effect was demonstrated based on measured PSF of the dark-field DHM system.

#549531 https://doi.org/10.1364/OPTCON.549531
Journal © 2025 Received 18 Nov 2024; revised 24 Jan 2025; accepted 27 Jan 2025; published 6 Feb 2025

OPTICS CONTINUUM

Figure 1(a) and (b) show two examples of this study where the variation in amplitude distribution affects the PSF, which characterizes the imaging properties such as crosstalk and resolution. The desired PSF for our imaging system has a homogeneous amplitude distribution, resulting in an Airy disk in the image plane [11]. This pupil amplitude distribution and PSF are presented in Fig. 1(c), and obtained by measuring with a 1 nm bandwidth filter. However, due to photon budget and a ideal coherence length of approximately 150 μm, quasi-monochromatic light is required in DHM for overlay metrology, resulting in spurious apodization.

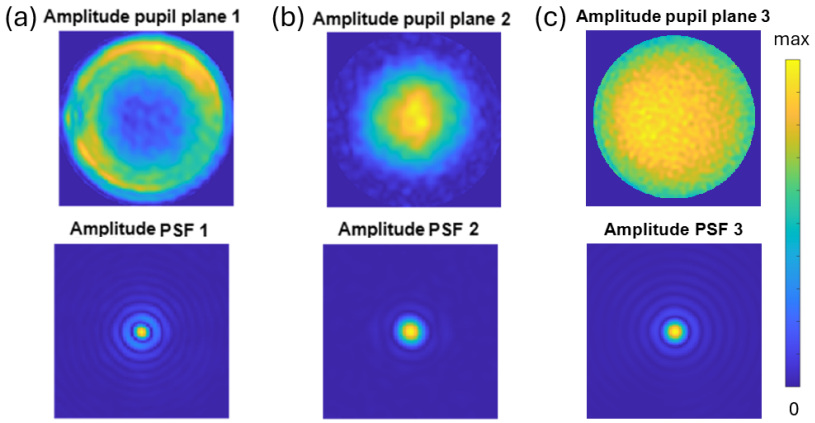

Fig. 1. (a) and (b) are two examples on the spurious apodization effects, where the measured amplitude distribution affects the imaging quality of the imaging system, demonstrated by the PSF, which was illuminated using a Gaussian spectral shape. [10]

Fortunately, this spurious apodization effect can be computationally corrected provided that we know the spectral shape of the light source. In Ref. [10], a Gaussian shape was assumed but there are plenty of cases where this assumption is not valid. For example, the quasi-monochromatic light generated by a supercontinuum source with an acousto-optic tunable filter (AOTF) can have a spectrum that significantly deviates from a Gaussian shape [12–15]. Therefore, the spectral shape needs to be accurately measured for the best possible computational correction of the spurious apodization.

The Fourier-transform (FT) spectrometer, that we will present in this paper, is ideally suited to measure the spectral shape of quasi-monochromatic light over a large range of wavelengths. Compared to conventional FT spectrometers, our FT spectrometer has no moving parts, is compact, low cost and can be calibrated with only one wavelength. Due to its simplicity and lack of moving parts, it can potentially be fabricated as a photonic integrated circuit, thereby minimizing the spectrometer's footprint. These features make it an attractive option for overlay metrology using DHM. Here, the required sub-nanometer metrology precision drives the need for near-perfect imaging conditions over a large range of wavelengths. The disadvantage of this FT spectrometer concept is that the OPD range limits the spectral resolution. For the application of overlay metrology the spectral resolution is far below what is needed, but for other application this might be a disadvantage.

In this paper, we present details on our FT-spectrometer concept, along with a description of a simple setup that we build for experimental validation. We will explain the concept and show experimental validation of this spectrometer. Finally, we will show how our FT-spectrometer is able to correctly predict spurious apodization in a DHM setup using light with a strong non-Gaussian spectral shape. We will use this spectrum-based calculation to correct the PSF of our DHM setup.

OPTICS CONTINUUM

2. Theory and system design

2.1. Concept FT-spectrometer

Our FT-spectrometer method is similar to the well-known Young's double-slit experiment [16] and is conceptually shown in Fig. 2 [17]. The two pinholes have a separation $2d$ and are placed along the x-axis. These pinholes are both illuminated by the same light source S. The light transmitted by the two pinholes propagate as diverging spherical waves that will overlap and interfere on the image sensor. There is a significant non-linear relation between the optical path length difference (OPD) of the two pinholes (x,y) position on the image sensor which is illustrated with the curved fringes in Fig. 2. However, this non-linear relation is well-defined and can be corrected. After a simple non-linearity correction, followed by a Fourier transform of the interferogram we obtain the source spectrum.

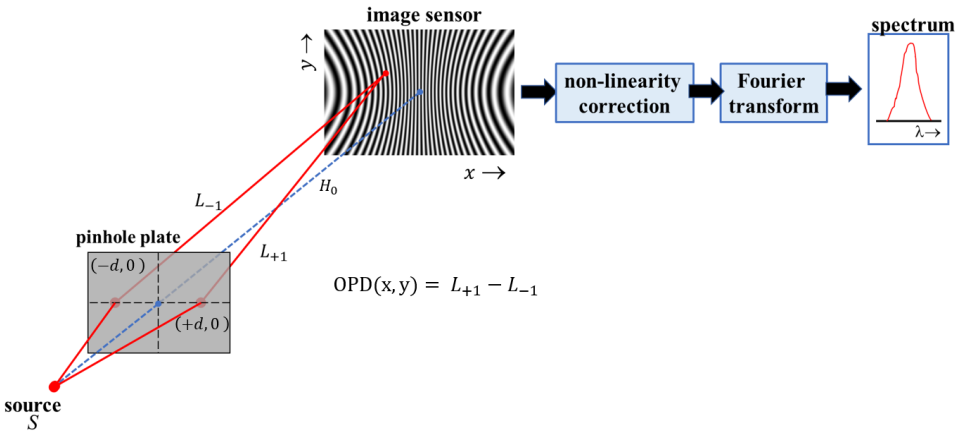

Fig. 2. Conceptual sketch of our FT-spectrometer. A light source S illuminates the two pinholes that generate two spherical waves that interfere on the image sensor. For the sake of clarity, the fringe density on the image sensor and its non-linear variation, due to the non-linear optical path length different (OPD), is shown highly exaggerated.

2.2. Theory

In this Fourier-transform spectrometer concept, the two spherical waves generated by the two pinholes interfere with each other at the camera sensor. The complex fields from the two pinholes can be expressed as,

$$E_{\pm 1} = \sqrt{I_S(k)}\sqrt{I_{\pm 1}}(x, y)\exp\left[-j2\pi k\, L_{\pm 1}(x, y)\right], \tag{1}$$

where -1 and $+1$ represent the left and right pinhole respectively, $I_S(k)$ is the source intensity at wavenumber $k = 1/\lambda$ and $I_{\pm 1}(x, y)$ describe a slowly varying relative intensity variation across the camera plane due to angle-dependent scattering from each pinhole. $L_{\pm 1}$ is the optical path length from each pinhole to a position (x, y) on the image sensor. The total intensity distribution on the image sensor is obtained by integrating over the entire source spectrum, given by

$$I(x, y) = \int_0^\infty |E_{+1} + E_{-1}|^2\, dk = \int_0^\infty I_S(k)\left[I_{+1} + I_{-1} + 2\sqrt{I_{+1}I_{-1}}\cos\left(2\pi k\mathrm{OPD}(x, y)\right)\right] dk. \tag{2}$$

The optical path difference is given by $\mathrm{OPD} = L_{+1} - L_{-1}$. In our setup, we eliminate the weak angle-dependent diffraction by also measuring the two fields on the image sensor separately. This

OPTICS CONTINUUM

allows us to obtain a background-free normalized interference signal, given by

$$I_N(x,y) = \int_0^\infty I_S(k)\cos\left[2\pi k \mathrm{OPD}(x,y)\right]dk. \tag{3}$$

In Eq. (3), the OPD variation across the camera location (x, y) is given by:

$$\mathrm{OPD} = \sqrt{(x+d)^2 + y^2 + H_0^2} - \sqrt{(x-d)^2 + y^2 + H_0^2}, \tag{4}$$

where the H_0 is the distance from the pinhole plane to the image sensor and $2d$ is the two pinholes spacing. In practice, the distance H_0 is much larger than the image sensor dimensions and pinholes spacing. Using the Taylor approximation $\sqrt{1+a} = 1 + (a/2) - (a^2/8)$ the OPD can be expressed as:

$$\mathrm{OPD} = \left(\frac{2d}{H_0} - \frac{d^3}{H_0^3} - \frac{dy^2}{H_0^3}\right)x - \frac{d}{H_0^3}x^3. \tag{5}$$

As shown in Fig. 2 and expressed in Eq. (5), a linear relation between OPD and the x-position on the camera sensor is obtained near the center of the image sensor. However, for large x-values a third order distortion becomes significant. Moreover, the OPD scaling is also weakly y-dependent.

The OPD expression of Eq. (5) assumes that the image sensor plane is perfectly aligned relative to the two pinholes. In reality, the image sensor can be slightly decentered over a distance S_x and S_y in, respectively the x- and y-direction. Moreover, the image sensor plane can also be tilted over small angles θ_x and θ_y around the x- and y-axis. Finally, the two pinholes can be slightly rotated over a small angle α around the z-axis. These small misalignment's create additional OPD variations across the image sensor area. Combining all misalignment terms, the optical path length for each individual pinhole can be expressed as,

$$L_{\pm 1} = \sqrt{(x \pm d + S_x)^2 + \left(y \pm \alpha d + S_y\right)^2 + \left(H_0 + x\theta_y + y\theta_x\right)^2} \tag{6}$$

Here, we assume that angular misalignment's are sufficiently small to use the well-known small angle approximation $\sin(a) = a$, $\cos(a) = 1$. These misalignment's in the setup can degrade accuracy and resolution of our spectrometer concept and must therefore be taken into account. The terms $S_{x,y}$, $\theta_{x,y}$ and α can be calibrated and included in the correction of the non-linear OPD variation across the image sensor plane. The calibration of H_0, d and the parameters that describe the small sensor misalignment's, S_x, S_y, θ_x, θ_y and α is done with a simple model-based iterative technique that needs only one accurately known wavelength (e.g. a HeNe laser) to determine the misalignment parameters. A detailed explanation of the calibration method using a HeNe source is presented in Appendix A.

3. Experiment

3.1. Experimental setup

In this section, we will describe the experimental setup used in this study. Fig. 3(a) shows a schematic drawing of the setup that was built to evaluate our FT-spectrometer concept. Light from a source is collimated with achromatic lens L1 (Thorlabs ACT508-200-A-ML, F=200 mm) and is sent to a regular Michelson interferometer configuration consisting of beam splitter (BS) and two mirrors (M3 and M4). These mirrors are tilted over an angle of approximately 0.48° resulting in two reflected beams that have opposite tilts.

Achromatic lens L2 (Thorlabs AC508-100-A-ML, F=100 mm) focuses these tilted beams on the two pinholes that have a diameter of 5 μm and a separation $2d$ of 4 mm. These pinholes were made in a 300 nm thick Chromium film on a glass substrate using a focused ion beam.

OPTICS CONTINUUM

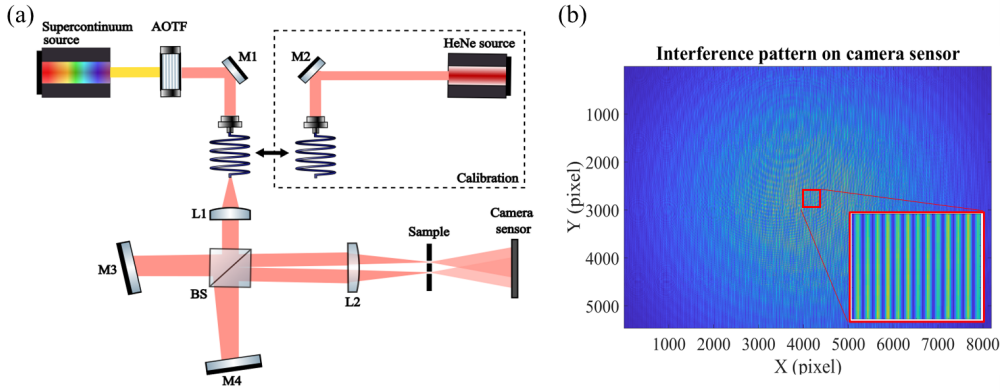

Fig. 3. (a) Schematic representation of the two pinhole FT-spectrometer setup.

The pinholes act as a spatial filter that improve the beam quality resulting in two well-defined diverging spherical beams that travel from the pinholes over a distance H_0 ($\approx$ 126 mm) towards the camera (Basler boA8100-16cm CoaXPress) that records the interference between the two spherical waves. The camera has an Onsemi XGS 45000 image sensor with a global shutter and 8192 (x-direction) $\times$ 5468 (y-direction) pixels with a pixel pitch of 3.2 μm. The HeNe laser source (Thorlabs HRS015B) shown in Fig. 3(a) is used to calibrate our FT-spectrometer. Further details of this calibration method are presented in the next section. The other source in Fig. 3(a) is a white light supercontinuum source (LEUKOS ROCK400-5) with two acoustic optical tunable filters (AOTF's) for wavelength selection covering the visible to near infrared wavelength range. Figure 3(b) shows an example of a measured interference pattern of the HeNe-laser calibration source before correction of the individual beam profiles. This setup is especially suited for high-brightness sources with a finite bandwidth like supercontinuum sources in combination with AOTF's that are used in our research on DHM for metrology applications.

3.2. *Non-linearity correction method*

Due to the non-linear OPD, described in section 2.2, the intensity of the interferogram is not purely sinusoidal but has multiple frequency components, as illustrated using a simulation in Fig. 4(a). Performing a Fourier transform over such a non-sinusoidal interferogram results in a broad undefined spectrum, as shown in Fig. 4(d), indicated in red. Linear interpolation is used to linearize the sample of the OPD, as shown in Fig. 4(b). Here, the non-equidistant dashed lines above represent OPD values that correspond to the pixels at location x in the detector array. The dashed lines below represent the OPD after linear interpolation. This non-linearity correction is performed in MATLAB using the standard interpolation function "interp1" with a spline fit. The interpolated interferogram now has a single frequency component as illustrated in Fig. 4(c). The corresponding Fourier transform of this interpolated interferogram then results in a single-peak spectrum as shown with the blue curve in Fig. 4(d).

To apply this non-linearity correction the system parameter are experimentally calibrated with a HeNe source. This calibration is presented in Appendix A. The non-linear correction method will be validated experimentally in the following section where we present the experimental results of this FT-spectrometer.

OPTICS CONTINUUM

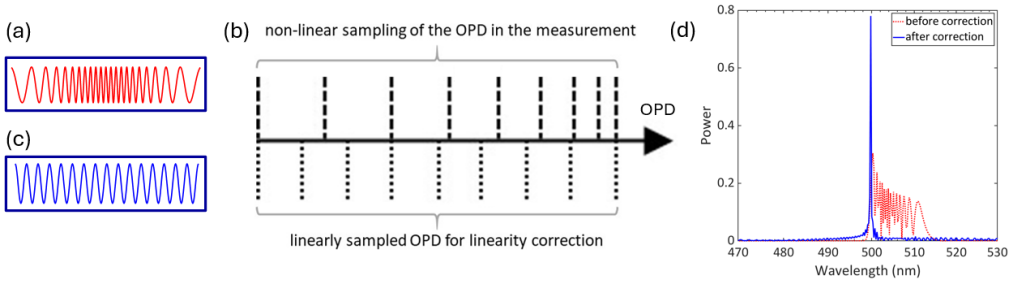

Fig. 4. Schematic illustration of the non-linearity correction using pixel interpolation. A simulation using Eq. (3) and Eq. (4) of the non-linear interference pattern (a) is linearized using non-linear sampling of the pixels (b) resulting in a linear interference pattern (c)

4. Results and discussions

Here, we verify the calibration by measuring the spectrum of a known bandwidth filter. We present first experimental data on the accuracy of the measured spectrum and show that our spectrometer can cover a large wavelength range. Finally, we will show how our FT-spectrometer is able to correctly predict spurious apodization in a DHM setup using light with a strong non-Gaussian shape. We will use this spectrum-based calculation to correct the PSF of our DHM setup.

4.1. Validation of calibration quality

After calibrating the system using a HeNe source and following the procedure as presented in Appendix A, the calibrated parameters are now used to correct the non-linear OPD variation in a spectrum measurement. To verify the calibration parameters, a 532-nm color filter with a 1 nm bandwidth is measured. From the non-linear corrected interferogram, each horizontal line can be Fourier-transformed resulting in a spectrum of the light source, as shown in Fig. 5(a). Therefore, also the consistency over the y-axis has been experimentally verified as presented in Fig. 5(b).

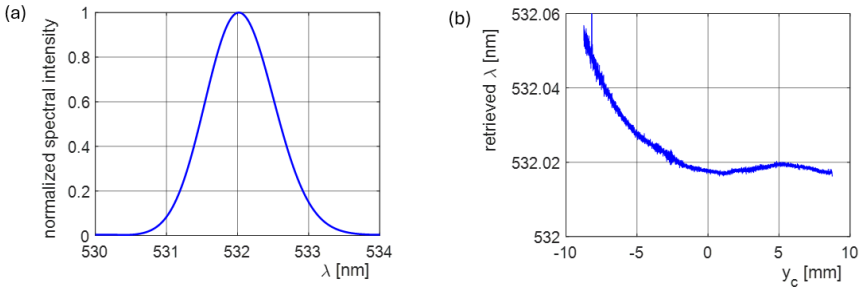

Fig. 5. (a) Retrieved spectra using middle row of the interferogram after non-linearity correction. (b) Measured error of the retrieved wavelength as function of y-position for a 532 nm source.

The retrieved central wavelength is equal to 532.0 ± 0.1 nm and the measured FWHM is 1.3 nm. The spectral resolution of this FT spectrometer with 8192 number of pixel in one line is 0.4 nm. The coherence length is proportional to $L_c \approx \frac{\lambda^2}{\Delta\lambda}$, which in our system is represented by the maximum OPD range. So, we can approximate the OPD range as OPD $\approx \frac{\lambda^2}{\Delta\lambda}$. Therefore, the spectral resolution of our FT spectrometer is approximately equal to $\Delta\lambda \approx \frac{\lambda^2}{\text{OPD}}$. With a measured wavelength of 532 nm and a OPD ranging from −400 to 400 μm, this results in a

OPTICS CONTINUUM

spectral resolution of $\Delta\lambda \approx \frac{0.532^2}{800} \cdot 10^3 = 0.4$ nm. Figure 5(b) shows the error of the retrieved central wavelength for a source with a 532 nm wavelength. The error is defined as the difference between the retrieved wavelength and the color filter 532 nm. Figure 5(b) shows that for most horizontal lines in the corrected interferogram array (the range of $-3<y<8$ mm) the retrieved central wavelength runs very smoothly with low noise per interferogram line. The error slightly increases towards y= −8 mm which can be attributed to the larger ΔOPD residuals that were observed in the top left image of the interferogram during the calibration, caused by spherical aberrations. These spherical aberrations could be caused by the relatively large diameter of the pinholes. A potential solution for this problem is described in section 5.

Next, the quality of our calibration methods was tested using a supercontinuum source equipped with two AOTF's (A and B). With these two AOTF's we generated quasi-monochromatic light in the range of 450 nm to 950 nm with 50 nm steps. For each programmed wavelength the central wavelength was measured using our FT-spectrometer.

The results of this wavelength range experiment are shown in Fig. 6. The FT-spectrometer shows small errors well below 1 nm over a wavelength range of 450 nm to 950 nm. So with one calibration wavelength our FT spectrometer can accurately measure over a broad wavelength range. Lastly, the results presented in Fig. 6 were obtained without readjusting optical elements as we changed the wavelength from 450 nm to 950 nm.

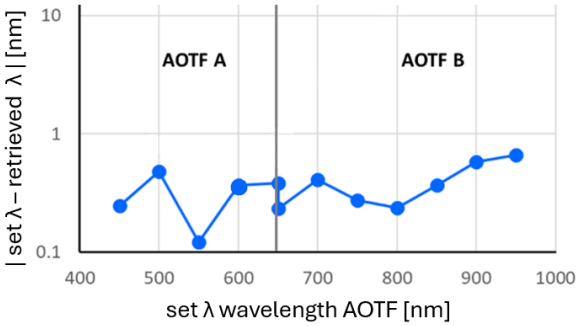

Fig. 6. (a) Measured wavelength error of our FT-spectrometer as a function of wavelength. The wavelengths of 450 nm – 650 nm were generated with AOTF-A and the wavelengths of 650 nm – 950 nm were generated with AOTF-B.

4.2. Computational spurious apodization correction

In DHM for overlay metrology, the spectral shape is determined by the acoustic optical tunable filter (AOTF). These AOTFs are commercially available, affordable, and offer fast color switching, making them suitable for high-throughput measurement applications, like overlay metrology. However, the complex non-linear acousto-optic interaction between the propagating optical and acoustical waves [18,19] can result in spectral line shapes that significantly deviate from the more common Gaussian or tophat-shaped filters. In coherent imaging systems such a non-Gaussian spectral line shape could result in spurious apodization effects affecting the image quality, as described in Ref. [10]. Here, the amplitude distribution in the pupil plane is directly related to the spectral shape. Therefore, accurate knowledge of the spectral characteristics of the illumination light source is required, and can allow for computational correction of this spurious apodization in DHM.

In this section, we will use our FT-spectrometer setup to measure the shape of the spectral transmission of an AOTF in more detail. The spectral shape of the AOTF depends on the wavelength and RF driving power. Variations in spectral shapes with different RF powers in an AOTF arise from non-linearity in acousto-optic interaction. Increasing the RF power amplifies

OPTICS CONTINUUM

the acoustic wave, affecting diffraction efficiency and the Bragg condition, which results in wavelength dependence. Moreover, material properties also behave non-linearly with RF power. In combination with localized heating from higher powers that alter the refractive index, this results in spectral shape which are highly dependent on wavelength and RF power [12–15]. Figure 7 shows the main findings of the AOTF characterization. The spectral shape is measured for programmed wavelengths of 550 nm (a-d), 650 nm (e-h) and 750 nm (i-l) with four different drive powers (4000, 5000, 6000 and 7000 mW). Especially at the longer wavelength (750 nm) we see that the spectral shape deviates significantly from the desired Gaussian or top hat shape. Moreover, the shape highly depends on the RF-drive power.

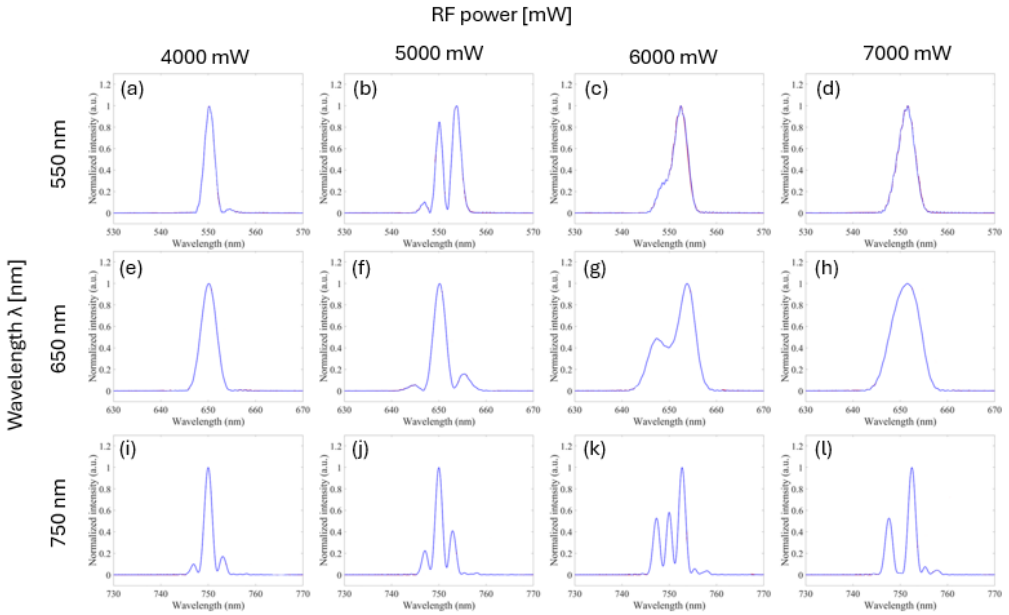

Fig. 7. Measured spectral transmission of our AOTF for 3 different wavelengths (a-d) 550 nm, (e-h) 650 nm and (i-l) 750 nm) for different radio-frequency (RF) drive powers (4000, 5000, 6000 and 7000 mW).

In Ref. [10] it was presented that the finite bandwidth of the light source in combination with a wavelength-dependent focal length of the imaging lens leads to a significant field-position dependent spurious apodization in our DHM setup. This significantly affects the aberration-corrected PSF in the DHM tool for overlay metrology. In that study, it was demonstrated that this spurious apodization, coming from an inhomogeneous amplitude distribution in the pupil plane, depended on the finite bandwidth of the source spectrum. In Ref. [10], for simplicity reasons, the spectral shape was assumed to be Gaussian. However, as shown in Fig. 7, the output spectrum of an AOTF is not a perfect Gauss-function and is highly dependent on wavelength and RF driving power [12–15]. Therefore, an accurate in-line spectrum measurement is important to allow a computational apodization correction to the levels of accuracy that is needed for demanding metrology applications. Such spectrum measurement can then be used to calculate the amplitude variation in the pupil plane and computationally correct for it. Figure 8 demonstrates this approach with experimental results. Here, a silicon sample with a nanohole, diameter 200 nm and depth 100 nm, is illuminated resulting in a scattering point source. The point source illuminates the lens aperture with a spherical wave. In case of a very narrow bandwidth (B < 1 nm), the amplitude in the exit pupil plane is a homogeneous distribution. For comparison, a measured pupil amplitude distribution of a 1 nm bandwidth filter was presented in Fig. 1(c).

OPTICS CONTINUUM

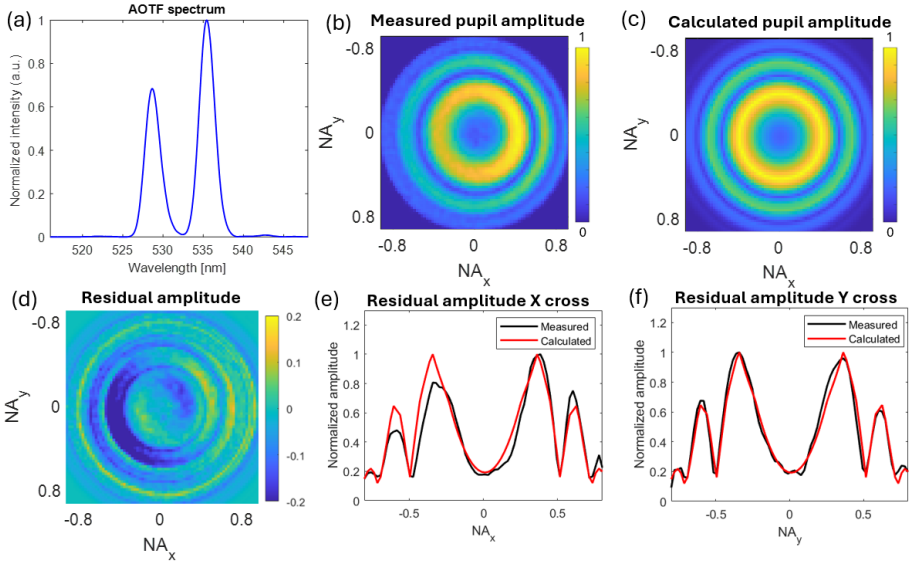

Fig. 8. Experimental correction of spurious apodization in DHM using the measured spectrum. (a) The measured non-Gaussian AOTF spectrum. (b) The measured pupil amplitude distribution. (c) The calculated pupil amplitude distribution based on the measured AOTF spectrum. (d) The residual amplitude distribution by subtracting (c) from (b). (e) and (f) show a x- and y- cross section of the residual amplitude, respectively.

However, when illuminating the nanohole with an non-Gaussian AOTF spectrum, Fig. 8(a), the measured pupil amplitude is a non-homogeneous distribution, as shown in Fig. 8(b). As mentioned before, the acousto-optic interaction in an AOTF is non-linear and far from trivial. Therefore, to perform the experimental demonstration of our correction method in a controlled manner, the non-Gaussian spectrum, as shown in Fig. 8(a), by combining two programmed wavelengths 529 nm and 536 nm both at a RF driving power of 4000 mW. As described in Ref. [10], the amplitude in the exit pupil plane can be expressed as,

$$A_{\mathrm{EP}}(\gamma) = \int_{-\infty}^{\infty} S(\Delta\lambda)\exp[i\gamma\Delta\lambda]d\Delta\lambda, \tag{7}$$

where $S(\Delta\lambda)$ is the source spectrum and γ a dispersion parameter. Using this expression the expected pupil amplitude distribution can be calculated based on the measured spectrum. The calculated pupil amplitude, using the measured spectrum (Fig. 8(a)), is presented in Fig. 8(c). A computational correction of the non-homogeneous pupil amplitude caused by spurious apodization is then performed by dividing the measured pupil amplitude by the calculated pupil amplitude,

$$A_{cor} = \frac{A_{meas}}{A_{calc}}. \tag{8}$$

The residual amplitude, i.e. the difference between the calculated A_{calc} and A_{meas} is presented in Fig. 8(d). Here, homogeneity in the amplitude distribution significantly improved after correction. Some residual amplitude variations are present caused by a small mismatch between the measured amplitude A_{meas} and the calculated amplitude A_{calc}. This mismatch is mainly related to the scattering profile of the nanohole. This scattering profile is observed in Fig. 8(b) as slightly more light in the right half of the pupil plane. This asymmetry is present in the x-direction, as shown in the x-cross section in Fig. 8(e), but is not present in the y-direction, as shown in the

OPTICS CONTINUUM

y-cross section in Fig. 8(f). In the y-direction, our calculated amplitude distribution matches the measured amplitude distribution very well. The nanohole's used in this study have a diameter of 200 nm, measured with a center wavelength of 532 nm. For a nanohole to scatter a perfectly spherical wavefront, the diameter should be much smaller than the measurement wavelength. In this study, the diameter of the nanohole is relatively large compared to the wavelength. Therefore, the scattering profile is not perfectly spherical but has some angular dependence in the x-direction. A smaller nanohole makes the scattering profile more symmetrical resulting in less residual artifacts. However, the smaller the nanohole the less light is scattered, resulting in more photon noise in the signal. Therefore, in this study a diameter of 200 nm was chosen accepting the imperfect scattering profile.

Back-propagating the measured and corrected complex-valued pupil planes to the image plane using an inverse Fourier transform, results in the PSF amplitude presented in Fig. 9(a) and (b), respectively. The spurious apodization lead to broadening of the sidelobs of the PSF as shown in Fig. 9(a). Correcting the pupil amplitude to a homogeneous amplitude distribution based on the source spectrum, results in a Airy disk function as shown in the Fig. 9(b). Figure 9(c) shows the cross section of (a) and (b) compared to the theoretical Airy disk function. There is a small mismatch visible between the corrected PSF cross section (red) and the theoretical cross section (black), which can be explained by the scattering profile of the nanohole as discussed earlier. Nevertheless, the accurately measured spectrum using our FT-spectrometer, allows for computational correction of the spurious apodization effect in DHM.

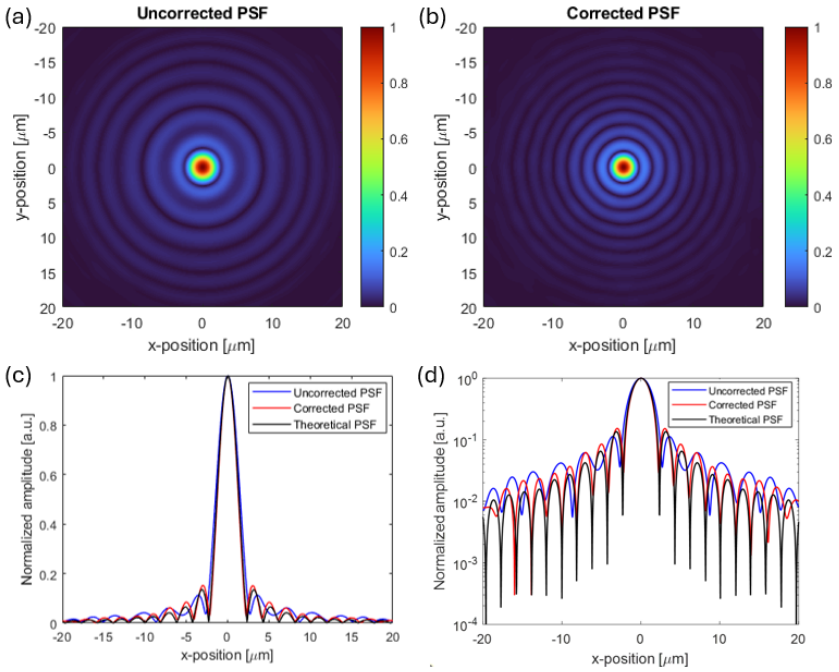

Fig. 9. The resulting PSF in the image plane before (a) and after (b) correction of spurious apodization in DHM using the measured spectrum. (c) shows the cross section of the uncorrected PSF (blue) and the corrected PSF (red) with respect to the theoretical Airy disk (black) and on logarithmic scale in (d).

OPTICS CONTINUUM

5. Future improvements

Future improvements: In this section, we will discuss the current limitations of the existing FT spectrometer setup and future improvements.

1. **Aberration minimization:** The main limitation of the current setup are aberrations caused by the relatively large pinhole diameter of 5 micrometer, which degrade fringe quality. As a future improvement, we plan to measure with smaller pinholes. A 1-micrometer pinhole would transmit a less aberrated wavefront, potentially enhancing fringe pattern quality. Additionally, developing an OPD model that accounts for aberrations would allow calibration of these effects as a system parameter, further minimizing their impact.
2. **DHM implementation:** In this study, the concept was experimentally validated using a PSF measurement. As a next step, we aim to measure an actual overlay target and enhance overlay retrieval through computational correction of spurious apodization. Thus far, spectral shape and PSF measurements were conducted sequentially. For overlay measurements, simultaneous spectrum and overlay target acquisition would be more advantageous. Figure 10 illustrates a potential implementation of the FT spectrometer within the df-DHM setup.
3. **Precision study:** The spectral resolution of 0.4 nm achieved with our FT spectrometer concept is currently limited by the OPD range and the finite number of pixels. The demonstrated sub-nm resolution is sufficient for various metrology applications, including semiconductor optical metrology tools. In our work, the number of pixels was constrained to 8192, but advances in image sensor technology are expected to provide sensors with more and smaller pixels, enabling further resolution improvements. Once higher resolution is achieved, a precision study with a detailed error analysis across the entire wavelength range would be valuable.

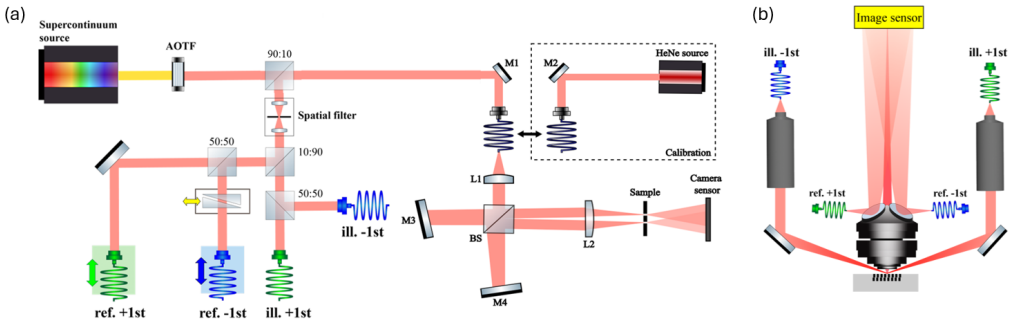

Fig. 10. A schematic representation of the FT spectrometer concept implemented in our df-DHM setup. (a) An AOTF selects the desired wavelength coming from the coherent white light source. A small portion of the light is split off and propagated to FT spectrometer. The other part of the beam is split in a reference and illumination beam by a 10:90 beamsplitter. 50:50 beamsplitters split the beam into two illumination and two reference beams. The two reference beam fibers are placed on a translation stage to create two delay lines. The beams are guided via polarization maintaining single mode fibers to the sensor head (b). The illumination beams are diffracted on the sample via an objective under an angle of 70°. The imaging lens captures both the $+1^{st}$ and -1^{st} diffraction orders. The diverging reference beams are reflected via a mirror on the camera.

Implementing these future improvements will overcome current limitations, enhance spectral resolution, reduce aberrations, and streamline measurement processes, ultimately advancing the capabilities and accuracy of the FT spectrometer.

OPTICS CONTINUUM

6. Conclusion

In this study, we have presented a simple and accurate spectrometer based on two interfering spherical beams. The FT-spectrometer can be calibrated using only one reference wavelength, while still accurately measuring over a large wavelength range. Moreover, our model-based calibration method is simple and robust against misalignment of the few parts in our FT-spectrometer. The sub-nm spectral resolution that we have demonstrated is sufficient for various applications including semiconductor optical metrology tools. We concluded the study with experimental work on spurious apodization correction using the measured spectrum in DHM for overlay metrology.

Appendix A : System parameter calibration

The calibration of H_0, d and the parameters that describe the small sensor misalignment's, S_x, S_y, θ_x, θ_y and α is done with a simple model-based iterative technique that is already well-established in semiconductor metrology applications like optical CD metrology [20]. Figure 11 presents a flow chart of our model-based calibration method.

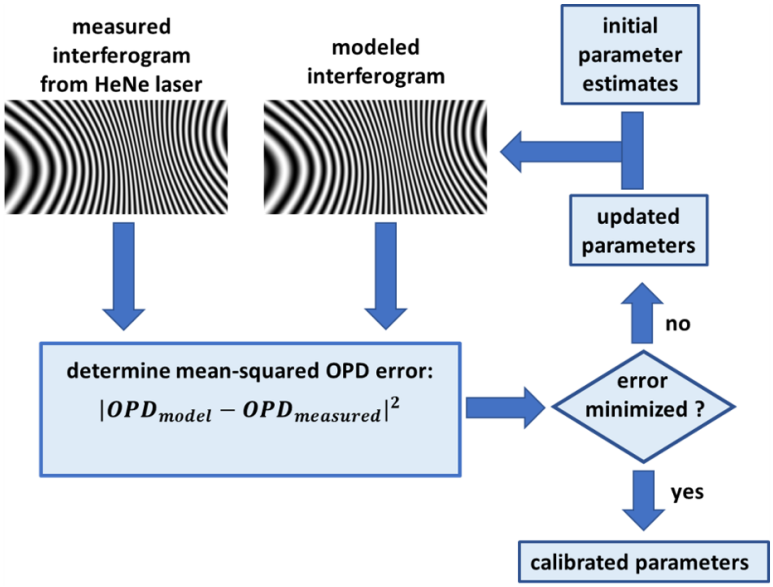

Fig. 11. Schematic flow chart of the model-based calibration method that was used to determine the parameters $S_{x,y}$, $\theta_{x,y}$, α, d and H_0.

Starting from a set of initial parameter estimates, a modeled interferogram is calculated using Eq. (6). A computational phase-stepping approach is then performed to calculate the difference between the OPD of the measured interferogram and the modeled interferogram. Based on the retrieved OPD difference, a new set of parameters is obtained and a new modeled interferogram is calculated. This loop is repeated until the mean-squared OPD difference (ΔOPD = OPD_{model} - $OPD_{measured}$) is minimized. This iterative minimization of the OPD error is fast and accurate since the model is based on simple free space propagation of spherical waves with only a few unknown model parameters. However, it assumes that these model parameters have different OPD-sensitivities. The parameter sensitivities of our FT-spectrometer concept are simulated using Eq. (6) for a pinhole separation $2d$ of 4 mm, a pinhole-image sensor distance H_0 of 125 mm. The simulation showed identical OPD sensitivity behavior for image sensor shift in the y-direction (S_y) and tilt around the x-axis (θ_x). These two misalignment's can therefore not be

OPTICS CONTINUUM

independently calibrated. However, sensor tilt has a much lower sensitivity than sensor shift. Therefore, we assume θ_x to be zero in our calibration.

For calibration of our FT-spectrometer three images are captured. First, we measure the interference pattern on the image sensor using the HeNe laser. Then also images of the individual pinholes, are measured to remove the amplitude envelope and DC background term from the interferogram. Our model-based calibration approach minimized the OPD difference ΔOPD between the measured and the modeled interferogram. Figure 12 shows this OPD difference at various stages the calibration process.

	before calibration	after calibration of H_0 and d	after full calibration
$\Delta OPD(x,y)$ [nm]	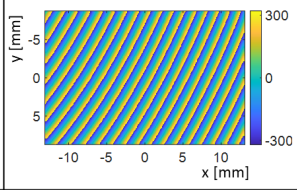	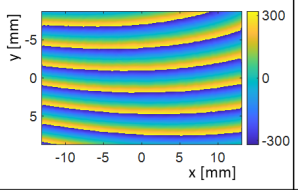	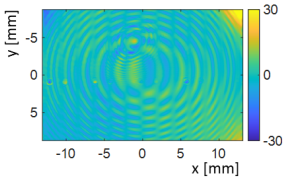
H_0 [mm]	125	127.160	127.160
d [mm]	2	2.009	2.009
S_x [mm]	0	0	1.29
S_y [mm]	0	0	-1.12
θ_y [mrad]	0	0	-9.6
α [mrad]	0	0	-7

Fig. 12. Difference between measured and modeled OPD at image sensor in various stages of the calibration steps. The table underneath the ΔOPD images shows the corresponding calibration parameters.

In Fig. 12, the left image shows the ΔOPD before any calibration has been applied. Here, the parameters are estimated such that the camera and pinholes are perfectly aligned and the the pinhole distance $2d$ equals the design value of 4 mm and the camera-pinhole distance is also equal to its intended value of 125 mm. A clearly visible x-gradient in the ΔOPD indicates that H_0 and/or d need to be adjusted. H_0 and d are then iteratively tuned until the linear x-gradient and the third order non-linearity are eliminated, resulting in the ΔOPD shown in the center image. After this first optimization in the model-based calibration the ΔOPD still contains a strong y-gradient and curvature. Therefore, the parameters $S_{x,y}$ (image sensor shift), θ_y (image sensor tilt) and α (pinhole rotation) are tuned iteratively, resulting in the right column of Fig. 12. After this model-based minimization of the ΔOPD a small residual ΔOPD in the range of a tens of nanometers is left. In the residual we clearly see two interleaved concentric rings that are almost certainly caused by spurious interference effects that are introduced by the cover glass that is in front of the image sensor. Moreover, in the residual ΔOPD small but significant ΔOPD values in the upper left and upper right corners are present. This could be caused by a small wavefront aberrations in the two interfering wavefronts. Generally, sufficiently low residual OPD errors were obtained after 10 to 20 iterations. The typical duration of a single calibration iteration on Intel Core i7-1185G7 CPU with 16 GB memory PC is a few seconds, resulting in a total processing time of several minutes.

Funding. Samsung (Advanced Research 362 Center for Nanolithography); University of Amsterdam; Rijksuniversiteit Groningen (RUG); Netherlands Organization 364 for Scientific Research (NWO); semiconductor-equipment manufacturer ASML.

Acknowledgements. The authors wish to thank Bartjan Spaanderman for support in building the setup and Bob Drent and Igor Hoogsteder of AMOLF for help in making the two pinhole sample.

OPTICS CONTINUUM

Disclosures. The authors declare no conflicts of interest. The authors declare that they have patents or patent applications. The authors Changmin Park and Youngseok Kang are employees of SAMSUNG. The authors Manashee Adhikary and Arie den Boef are employees of ASML.

Data availability. Data underlying the results presented in this paper are not publicly available at this time but may be obtained from the authors upon reasonable request.

References

1. X. Quan, D. Kato, V. Daria, *et al.*, "Holographic microscope and its biological application," Neurosci. Res. **179**, 57–64 (2022). Lighting up cosmic neuronal networks with transformative in vivo calcium imaging.
2. T. Baumbach, W. Osten, C. von Kopylow, *et al.*, "Remote metrology by comparative digital holography," Appl. Opt. **45**(5), 925–934 (2006).
3. G. Pedrini, P. Fröning, H. Fessler, *et al.*, "In-line digital holographic interferometry," Appl. Opt. **37**(26), 6262–6269 (1998).
4. Y. Emery, T. Colomb, and E. Cuche, "Metrology applications using off-axis digital holography microscopy," J. Phys. Photonics **3**(3), 034016 (2021).
5. T. T. van Schaijk, C. Messinis, N. Pandey, *et al.*, "Diffraction-based overlay metrology from visible to infrared wavelengths using a single sensor," J. Micro/Nanopattern. Mats. Metro. **21**(01), 014001 (2022).
6. M. Adhikary, T. van Gardingen-Cromwijk, J. de Wit, *et al.*, "Illumination spot profile correction in digital holographic microscopy for overlay metrology," J. Micro/Nanopattern. Mats. Metro. **22**(02), 024001 (2023).
7. T. van Gardingen-Cromwijk, S. Mathijssen, M. Noordam, *et al.*, "Enhancing diffraction-based overlay metrology capabilities in digital holographic microscopy using model-based signal separation," Accepted for publication in the Journal of Micro/Nanopatterning, Materials, and Metrology (2024).
8. C. Messinis, "Dark-field digital holographic microscopy for advanced semiconductor metrology," Phd-thesis - research and graduation internal, Vrije Universiteit Amsterdam (2022).
9. T. van Gardingen-Cromwijk, S. Konijnenberg, W. Coene, *et al.*, "Non-isoplanatic lens aberration correction in dark-field digital holographic microscopy for semiconductor metrology," Light: Adv. Manufact. **4**(4), 1 (2023).
10. T. van Gardingen-Cromwijk, M. Adhikary, C. Messinis, *et al.*, "Field-position dependent apodization in dark-field digital holographic microscopy for semiconductor metrology," Opt. Express **31**(1), 411–425 (2023).
11. C. Bennett, *Principles of Physical Optics* (Wiley, 2022).
12. A. Mahieux, V. Wilquet, R. Drummond, *et al.*, "A new method for determining the transfer function of an acousto optical tunable filter," Opt. Express **17**(3), 2005–2014 (2009).
13. G. Georgiev, D. A. Glenar, and J. J. Hillman, "Spectral characterization of acousto-optic filters used in imaging spectroscopy," Appl. Opt. **41**(1), 209–217 (2002).
14. C. Stedham, M. Draper, J. Ward, *et al.*, "A novel acousto-optic tunable filter for use in hyperspectral imaging systems," in *Physics and Simulation of Optoelectronic Devices XVI*, vol. 6889 M. Osinski, F. Henneberger, and K. Edamatsu, eds., International Society for Optics and Photonics (SPIE, 2008), p. 68891C.
15. E. G. Bucher and J. W. Carnahan, "Characterization of an acousto-optic tunable filter and use in visible spectrophotometry," Appl. Spectrosc. **53**(5), 603–611 (1999).
16. T. Young, "I. the bakerian lecture. experiments and calculations relative to physical optics," Philos. Trans. R. Soc. London **94**, 1–16 (1804).
17. A. den Boef, P. van Schaijk, I. Setija, *et al.*, "Method and apparatuses for fourier transform spectrometry," (2024). WIPO International Application No. PCT/EP2023/067754.
18. S. N. Mantsevich, V. I. Balakshy, K. B. Yushkov, *et al.*, "Quasi-collinear aotf spectral transmission under temperature gradients aroused by ultrasound power absotption," IEEE Trans. Ultrason., Ferroelect., Freq. Contr. **69**(12), 3411–3421 (2022).
19. A. Korpel, *Acousto-optics*, vol. 57 (CRC Press, 1996).
20. X. Niu, N. Jakatdar, J. Bao, *et al.*, "Specular spectroscopic scatterometry," IEEE Trans. Semicond. Manufact. **14**(2), 97–111 (2001).